36M-pixel synchrotron radiation micro-CT for whole secondary pulmonary lobule visualization from a large human lung specimen

Keiji Umetani [a,*], Toshihiro Okamoto [b], Kurumi Saito [c], Yoshiki Kawata [c], Noboru Niki [c]

[a] *Spectroscopy and Imaging Division, Japan Synchrotron Radiation Research Institute, 1-1-1 Kouto, Sayo-cho, Sayo-gun, 679-5198, Hyogo, Japan*
[b] *Department of Thoracic and Cardiovascular Surgery, Cleveland Clinic, Cleveland, OH, USA*
[c] *Department of Optical Science and Technology, Faculty of Engineering, Tokushima University, Tokushima, Japan*

ABSTRACT

A micro-CT system was developed using a 36M-pixel digital single-lens reflex camera as a cost-effective mode for large human lung specimen imaging. Scientific grade cameras used for biomedical x-ray imaging are much more expensive than consumer-grade cameras. During the past decade, advances in image sensor technology for consumer appliances have spurred the development of biomedical x-ray imaging systems using commercial digital single-lens reflex cameras fitted with high megapixel CMOS image sensors. This micro-CT system is highly specialized for visualizing whole secondary pulmonary lobules in a large human lung specimen. The secondary pulmonary lobule, a fundamental unit of the lung structure, reproduces the lung in miniature. The lung specimen is set in an acrylic cylindrical case of 36 mm diameter and 40 mm height. A field of view (FOV) of the micro-CT is 40.6 mm wide × 15.1 mm high with 3.07 μm pixel size using offset CT scanning for enlargement of the FOV. We constructed a 13,220 × 13,220 × 4912 voxel image with 3.07 μm isotropic voxel size for three-dimensional visualization of the whole secondary pulmonary lobule. Furthermore, synchrotron radiation has proved to be a powerful high-resolution imaging tool. This micro-CT system using a single-lens reflex camera and synchrotron radiation provides practical benefits of high-resolution and wide-field performance, but at low cost.

1. Introduction

The secondary pulmonary lobule, the smallest functionally complete and fundamental unit in the lung [1–3], is separated from neighboring secondary pulmonary lobules by interlobular connective tissue septa. The lobule, which has irregular polyhedral shapes of 5–30 mm diameter, includes numerous alveoli by which gases are exchanged with surrounding capillaries of less than 10 μm diameter. The secondary pulmonary lobule reproduces the lung in miniature. Therefore, recognition of the structure of the whole secondary pulmonary lobule can be expected to elucidate the entire lung structure.

Synchrotron radiation micro-CT has proved to be a powerful high-resolution lung specimen imaging tool [4,5]. Human lung specimens are regarded as in vivo human lungs to the greatest extent possible, with preserved lung structure [6]. Three-dimensional (3-D) imaging of a whole secondary pulmonary lobule specimen with spatial resolution of around 5 μm reveals micro-architectures ranging from airways, arterioles, venules, and lymphatics to alveoli and the associated pulmonary capillary bed. Recognition of abnormalities affecting the capillary

anatomy of the alveolar walls can clarify the relation between the architectures and abnormalities related to lung disease mechanisms. Nevertheless, the standard synchrotron radiation micro-CT setup does not accommodate the field of view (FOV) and spatial resolution requirements for human-lung specimen imaging applications targeting visualization of the whole secondary pulmonary lobule [7–9] because many are extremely high-priced devices incorporating very expensive scientific grade cameras and because many are not easily remodeled to achieve higher performance without entailing much higher costs.

At SPring-8 over a decade ago, a micro-CT system based on a 10M-pixel scientific-grade CCD camera with approximately 7 μm spatial resolution was developed for 3-D specimen imaging of centimeter-sized objects [10]. Subsequently, more recent studies have required systems with higher spatial resolution and a wider FOV. Nevertheless, high-megapixel scientific-grade cameras used to develop a new micro-CT system with several tens of megapixels are extremely expensive. From the early 2010s, consumer-grade camera manufacturers have offered ever larger pixel counts for their newer models. High megapixel digital single-lens reflex cameras have come to be used for cost-effective

special-purpose x-ray imaging [11–14]. Research has also revealed that low-cost consumer-grade cameras have excellent noise performance compared to expensive scientific-grade CCD cameras. Moreover, advancement of consumer grade camera technology has occurred more rapidly than that of scientific grade camera technology because consumer-grade camera manufacturers have larger R&D systems and commodity markets than scientific-grade camera firms do.

We have been developing large-field and high-resolution micro-CT systems using consumer-grade single-lens reflex cameras with a complementary metal oxide semiconductor (CMOS) sensor. The systems are specialized for large human lung specimen imaging. First and second prototype micro-CT systems were developed in a cost-effective manner using a 36M-pixel camera to confirm that they meet the demanded performance specifications: higher spatial resolution and a wider FOV than those of the 10M-pixel micro-CT system [15]. Then, a third system using the 36M-pixel camera was developed for practical use to visualize the 3-D structure of whole secondary pulmonary lobule specimens [16]. A large lung specimen is set in an acrylic cylindrical case of 36 mm diameter and 40 mm height. However, in an early stage of lung specimen imaging at SPring-8, each specimen was cut down to a cylindrical sample with 6 mm diameter and 15–25 mm height [7].

This paper describes the current performance of the wide-field and high-resolution 36M-pixel micro-CT system. First, wide-angle lenses for wide field imaging produce a barrel distortion, which can be measured by taking an x-ray image of an aluminum plate chart that includes a pattern with aligned holes. Second, spatial resolutions were evaluated quantitatively. After modulation transfer functions (MTF) of CT reconstruction images were obtained using a tungsten wire phantom, they were compared with those of the 10M-pixel system that had been already replaced by the cost-effective 36M-pixel CT system. Third, we considered the CT image quality of the human lung specimen based on contrast agent perfusion. Many studies [4,5,7–9] have concentrated on 3-D CT imaging of lung specimens down to small blood vessels without the need for contrast agent infusion. Apart from lung specimens, synchrotron radiation micro-CT is used widely for imaging of biomedical specimens of many kinds based on contrast agent perfusion [17–20]. For this study, barium sulfate particles were administered to the lung blood vessels as a contrast agent. Barium sulfate particles were suspended in buffer saline. Human lung specimens were inflated and fixed using Heitzman's method [6] after contrast agent injection into blood vessels. We considered the relation between the CT image quality and the barium sulfate particle density in the contrast agent, aiming at achieving 3-D visualization of capillaries in the alveolar walls.

2. Material and methods

2.1. Imaging system

Imaging experiments were conducted at the SPring-8 BL20B2 beamline presented in Fig. 1 (lower) [16]. A useful source of synchrotron radiation is a storage ring, which uses many bending magnets to maintain an electron beam at relativistic speeds in a closed trajectory. Only one bending magnet is depicted in Fig. 1. By bending the electron path, x-rays are emitted at each bending magnet in a direction that is tangential to the beam trajectory. Synchrotron radiation consists of broad-spectrum x-rays. A double-crystal monochromator selects a single energy of white synchrotron radiation. The monochromatic x-ray energy was therefore adjusted by the monochromator to 15–25 keV to produce high-contrast images of the lung specimens.

Human lung specimens are obtained from rejected donor lungs in Cleveland, Ohio. Lungs are procured with the clinical standard protocol. Following antegrade flush of the pulmonary artery with 4 L of Perfadex (XVIVO Perfusion Inc., Englewood, CO, USA), pulmonary veins were retrogradely flushed with 2 L of Perfadex and stored on ice for 4−10 hours. The pulmonary artery was flush with 1 L of 30°C Bamster solution (contrast agent, Barium Sulfate, Kaigen Phrama Co., Ltd., Osaka, Japan; diluted 2–50 times with saline). The pulmonary artery pressure is kept at 50 mmHg and lungs are ventilated with tidal volume 6 mL/ideal body weight, respiratory rate 7/min, PEEP 5 cmH$_2$O, and FiO$_2$ 0.4. Then, lungs are fixed using Heitzman's method [6]. This study is approved by Cleveland Clinic Institutional Review Board.

SPring-8 is a large-scale facility. The full length of the BL20B2 beamline is 215 m from the bending magnet to the detector. The micro-CT system was assembled on the lowermost stream side in Fig. 1 (lower). The point of strongest synchrotron radiation is a nearly parallel x-ray beam. The advantages of synchrotron radiation micro-CT compared with conventional cone-beam micro-CT [21] include the following: the monochromatic x-ray beam prevents beam-hardening artifacts; also, the
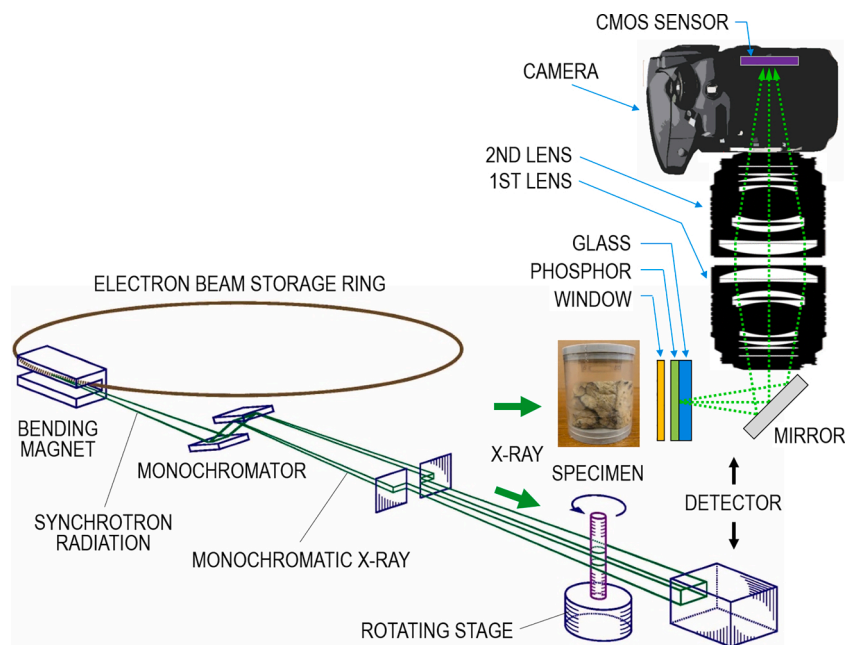
Fig. 1. (lower) Experiment setup for the synchrotron radiation micro-CT at the SPring-8 BL20B2 beamline and (upper right) cross-section of the high megapixel x-ray detector for large human-lung specimen imaging using a low-cost consumer-grade camera.

use of a nearly parallel beam enables exact CT reconstruction.

The x-ray detector uses an indirect conversion approach to detect x-ray images. Fig. 1(upper right) displays a cross-section of optical components of the x-ray detector and shows how light passes through the optical assembly. In the indirect conversion approach, a phosphor converts the x-rays into light, which a CMOS image sensor in the camera subsequently converts into a charge. The detector includes the phosphor screen, an optical mirror, a coupling lens consisting of a pair of first and second lenses, and the 36M-pixel CMOS camera. X-rays are converted into a visible image on the 6-µm-thick phosphor screen. The mirror behind the screen deflects the luminescent light 90 deg upward to the coupling lens, which then focuses it onto the CMOS sensor. This deflection is done to protect the lenses and the camera from direct x-ray exposure. The camera (D800e; Nikon Corp., Tokyo, Japan) is fitted with a CMOS sensor that has a 35.9 mm wide × 24.0 mm high active area. The CMOS has 7360 × 4912 pixels, each of which is 4.88 µm × 4.88 µm.

The phosphor screen unit includes a 0.1-mm-thick aluminum window for x-ray incidence. The phosphor layer is deposited on an optical glass immediately behind the window. The phosphor is a terbium-doped gadolinium oxysulfide (Gd_2O_2S:Tb) scintillator. The spatial resolution depends strongly on the phosphor screen thickness. Therefore, the 6-µm thick phosphor screen was attached to the micro-CT system to achieve detector resolution of around 5 µm, which is comparable to the CMOS sensor pixel size of 4.88 µm. In the tandem lens configuration of the coupling lens, the optical system comprises a pair of single-lens reflex camera lenses arranged face-to-face. The phosphor screen is placed in the focal plane of the first lens, whereas the image sensor is placed in the focal plane of the second lens. The optical magnification in the tandem lens system is ascertained from the ratio of the second lens focal length to that of the first lens. The FOVs and pixel sizes of x-ray detectors are determined by the optical magnification in the tandem lens system. Table 1 presents specifications of the two imaging modes of the present 36M-pixel system and the standard mode of the former 10M-pixel system using a scientific-grade CCD camera (C4742−95R; Hamamatsu Photonics K.K., Shizuoka, Japan) [10]. The 10M-pixel system, a commercial product, consists of the fixed no-magnification lens combination.

A standard optical system in Fig. 1(upper right) comprises first and second lenses with equal 135 mm focal length (AI AF DC-Nikkor 135 mm f/2D; Nikon Corp., Tokyo, Japan) and with a fixed focal-length ratio of one to one. The CMOS sensor pixel has dimensions of 4.88 µm × 4.88 µm. An equivalent pixel size projected onto the phosphor screen area is

an identical value of 4.88 µm on a side because the magnification factor of the coupling lens system is 1.0. The x-ray FOV is also 35.9 mm × 24.0 mm. The FOV is sufficiently adaptable to wide field imaging to obtain a three-dimensional CT image of the whole secondary pulmonary lobule.

By changing the lens combination, widely various magnifications are readily obtainable for high-resolution imaging. In high-resolution mode, the optical system comprises the first lens with 85 mm focal length (AF—S Nikkor 85 mm f/1.4; Nikon Corp., Tokyo, Japan) and the second lens with 135 mm focal length. In this case, an equivalent pixel size projected onto the phosphor screen area is 3.07 µm on a side because the magnification factor of the coupling lens system is 1.59. The x-ray FOV also decreases to 22.6 mm × 15.1 mm.

2.2. Offset CT scanning

The lung specimen, set in an acrylic cylindrical case with 36 mm diameter and 40 mm height, was placed on the rotating stage as depicted in Fig. 1. In the present 36M-pixel system, the detector's x-ray FOVs are, respectively, 35.9 mm × 24.0 mm and 22.6 mm × 15.1 mm with coupling-lens magnification factors of 1.0 and 1.59. In a standard CT imaging mode with 4.88 µm pixel size, the specimen fits within the detector's horizontal FOV (35.9 mm × 24.0 mm). Projection images were acquired over an angular range of 180 deg with an angular step of 0.1 deg or 0.05 deg.

In a high-resolution imaging mode with 3.07 µm pixel size, micro-CT imaging must be performed for the lung specimen beyond the detector's horizontal FOV (22.6 mm × 15.1 mm). We used offset CT scanning, which meets the requirement that the imaging region of the scanned specimen must fit within a small FOV [9,22,23]. The center of the stage rotation is deviated from the center of the detector's horizontal FOV; it is located near the FOV edge. Offset scanning involves 360 deg rotation of the rotating stage with an angular step of 0.1 deg or 0.05 deg. The fundamental idea of reconstruction from the offset scanning is to reorganize the incomplete projections into complete parallel-beam projections by the image combination [16]. The scan FOV using the offset scanning is approximately twice as large as the FOV of 22.6 mm × 15.1 mm. Specifications of the two scanning types are presented in Table 2.

In the normal scanning, image signals are converted to digital data with a 7360 × 4912-pixel, 14-bit format by an analog-to-digital converter in the camera. In the offset scanning, image signals are converted and eventually combined into digital data with a 13,220 × 4912-pixel, 14-bit format. However, the numeric value of 13,220 is not fixed. The number of pixels in the horizontal direction varies to some degree depending on the image combination process. For image acquisition, a personal computer system controls the camera using camera software (Camera Control Pro 2; Nikon Corp., Tokyo, Japan) and the rotating stage for acquiring projection images from multiple directions.

2.3. Distortion

A photograph should be a perfect to-scale representation of the x-ray image on the fluorescent screen. However, wide-angle lenses for wide-field imaging generally produce a barrel distortion, which affects mapping: an image is mapped around a sphere or barrel, leading to less than ideal mapping [24]. Particularly, unlike conventional photographic

Table 1
Camera and detector specifications for micro-CT systems.

Camera	Sensor	36M CT CMOS		10M CT CCD
	Total pixels	36.15 M		10.50 M
	Active pixels	7360 × 4912		4000 × 2624
	Pixel size [µm]	4.88		5.87
	Active area [mm]	35.9 × 24.0		23.6 × 15.5
	Readout [bit]	14		12
X-ray Detector	Mode	Standard	High-resolution	Standard
	Phosphor Thickness [µm]	6	6	10
	Lens system	No magnification	Magnification	No magnification
	1st lens focal length [mm]	135	85	105
	2nd lens focal length [mm]	135	135	105
	Magnification factor	1	1.59	1
	Pixel size [µm]	4.88	3.07	5.87
	Field of view [mm]	35.9 × 24.0	22.6 × 15.1	23.6 × 15.5

Table 2
Fields of view and pixel sizes of the normal and offset scanning in the 36M-pixel CT system.

	Normal scan	Offset scan
Field of view [mm]	22.6 × 15.1	40.6 × 15.1
Active pixels	7360 × 4912	13,220 × 4912
Total pixels	36.15 M	64.94 M
Pixel size [µm]	3.07	3.07
Specimen rotation [deg]	180	360

cameras, the x-ray detector comprises two lenses. The distortion can be measured by taking an x-ray image of an aluminum plate chart that includes a pattern with aligned holes. The pattern is a two-dimensional lattice shape array of 50-μm-diameter holes spaced uniformly at 1.0-mm intervals in the 500 μm thick plate. The machining accuracy of the drilling hole array is about 10 μm. The lens distortion is measured by the extent to which the observed holes deviate from the straight alignment of the pattern.

2.4. Modulation transfer function

The 36M-pixel micro-CT allows for the noninvasive imaging of the internal microstructure of lung specimens with isotropic spatial resolution in the range of several micrometers. Therefore, quantitative characterization of the performance of the micro-CT is important for evaluating the accuracy of size measurement of fine details in micro-CT images. The MTF in the scanning plane (transversal direction) is generally calculated as the absolute value of the normalized Fourier transform from the point spread function (PSF) obtained by scanning a thin wire phantom. Because the wire is not a point source, the raw MTF is corrected for the finite size of the wire phantom [25–27]. We applied the method to tungsten wire images obtained using the present 36M-pixel system and the former 10M-pixel system [28,29].

Fig. 2 presents a tomographic slice in the transversal direction of the micro-wire phantom consisting of 3, 10, and 30 μm diameter wires obtained using the 10M-pixel system. The wires were perpendicular to the CT scan plane. Fig. 2 depicts cross-sections of the three wires, a support frame for the wires (SF), and an acrylic cylindrical case (CASE). The phantom was scanned with x-ray energy of 15 keV, providing data for a 4000 × 4000 × 2624 voxel image with 5.87 μm isotropic voxel size. The 1800 projections were acquired over an angular range of 180 degrees with angular steps of 0.1 degrees. Because the monochromatic x-ray beam is regarded as a parallel beam, the reconstruction was made with a filtered backward-projection algorithm using a Shepp–Logan filter [30].

Thin, bright and dark streaks appeared preferentially in the vertical direction in Fig. 2. Thicker wires have stronger streak artifacts. Larger cross-sections have a longer range of the streak. They are caused by the presence of strongly attenuating objects such as tungsten wires. To resolve this difficulty, several approaches might be used with less-attenuating materials, smaller cross-section devices, and higher-energy x-rays [31,32]. The phantom was scanned with x-ray energy of 15

keV. An important advantage of the synchrotron radiation micro-CT is that the double-crystal monochromator can select a single energy of white synchrotron radiation in Fig. 1. The monochromatic x-ray energy can therefore be adjusted by the monochromator to 15–25 keV to produce high-quality x-ray images. The phantom in Fig. 2 was scanned using x-ray energy of 15 keV. Then, the x-ray energy was adjusted by the monochromator to 20 keV to prevent streak artifacts [28].

3. Results

3.1. Distortion

In lens optics, the image brightness at the image edge is reduced by a shading effect compared to the image center. The shading effect, which is sensitive to the lens aperture, is much larger for small F-number lenses. The high-resolution mode of the 36M-pixel system consists of two lenses: the first with 85 mm focal length and 1.4 F-number and the second with 135 mm focal length and 2.0 F-number. Distortion is also sensitive to the lens aperture; it is much larger in lenses with a small F-number. The x-ray detector consists of two lenses, unlike conventional photograph cameras.

Fig. 3(a) displays an x-ray image of the aluminum plate chart with the pattern of aligned holes taken using the 36M-pixel system with x-ray energy of 20 keV. The image has non-uniformity of brightness. For CT reconstruction, flat-field correction to the projection images is applied to compensate for variations in the pixel-to-pixel gray values caused by the pixel-to-pixel sensitivity of the image sensor and x-ray beam inhomogeneity. In conventional flat field correction, projection images without an object are acquired. They are designated as calibration images. A flat-field corrected projection image is produced by dividing the raw projection image by the calibration image. A flat-field corrected image is shown in Fig. 3(b). An intensity profile is superimposed on the backward corrected image to generate the composite image in Fig. 3(b). The intensity profile consists of single pixel gray values along the upper
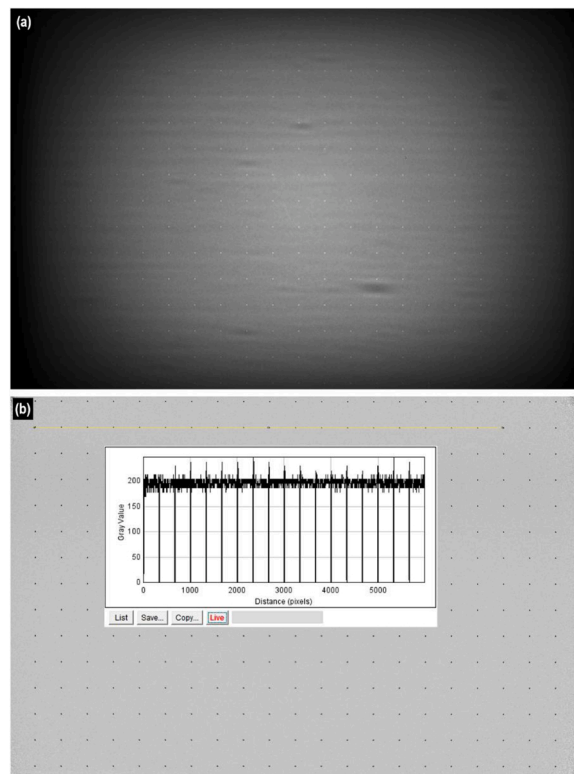

Fig. 2. Tomographic slice in the transversal direction of the micro-wire phantom consisting of 3, 10, and 30 μm diameter wires.

Fig. 3. X-ray images of the aluminum plate chart with the pattern of aligned holes.

yellow straight line on the backward corrected image. As a result of the measurement, no distortion was observed over the entire image within the measurement error range. Therefore, distortion correction operations were unnecessary before the CT reconstruction operation.

3.2. MTF

Point spread functions were obtained from transversal tomographic slice images of the 3-μm-diameter wire using the present 36M-pixel CT system and the former 10M-pixel CT system with x-ray energy of 20 keV. The thin wire phantom is positioned as perpendicular to the transverse plane. The MTF values were obtained by Fourier transform of the point spread functions calculated from the tomographic slice images [28,29]. The high-resolution and standard modes were used respectively for the 36M-pixel and 10M-pixel CT systems in Table 1. Fig. 4 presents the in-plane MTFs calculated from each slice image. Red and blue curves respectively represent the Fourier transform results obtained using the 36M-pixel and 10M-pixel CT systems. Table 3 presents spatial resolution values of the 36M-pixel and 10M-pixel CT denoted by units of [cycle/mm] and [μm] in the case of 10 % MTF and 5 % MTF.

3.3. CT images

Human lung specimens were inflated and fixed using Heitzman's method [6] after contrast agent injection into blood vessels to visualize micro-architectures ranging from airways, arterioles, venules, and lymphatics to alveoli and the associated pulmonary capillary bed. Small blood vessels were well filled with the barium sulfate microparticle contrast agent to obtain detailed 3-D representations of morphology of the vascular system. They are set as in vivo human lungs to the greatest degree possible, with preservation of the lung structure.

In micro-CT imaging, the lung specimen was set in the acrylic cylindrical case with 36 mm diameter and 40 mm height. The acrylic case was placed on the specimen rotating stage in Fig. 1. Monochromatic x-ray energies were adjusted by the monochromator to 20 and 25 keV to evaluate the x-ray energy dependence of tomographic image quality. Micro-CT imaging was performed in the high-resolution imaging mode with 3.07 μm pixel size using offset CT scanning. In all, 7200 raw projection images were acquired over an angular range of 360 deg with an angular step of 0.05 deg. The incomplete projections in the offset CT scanning were reorganized into complete parallel-beam projections. The CT images were reconstructed using the conventional back projection algorithm with the Shepp–Logan filter [30]. Then, we obtained the 3-D isotropic volumetric data (13,220 × 13,220 × 4912 voxels) stacking the two-dimensional CT slice images with voxel resolution of 3.07 μm × 3.07 μm × 3.07 μm.
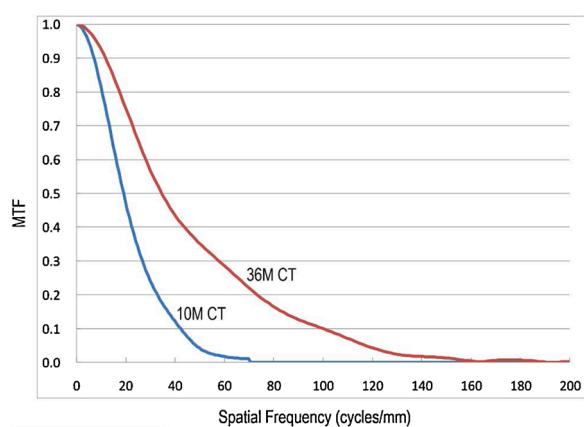

Fig. 4. MTF results obtained using the 36M-pixel (red curve) and 10M-pixel (blue) CT systems. (For interpretation of the references to colour in the Figure, the reader is referred to the web version of this article).

Table 3
Spatial resolution values of the 36M-pixel and 10M-pixel CT.

|	MTF 10 %		MTF 5 %		Pixel size
	[cycle/mm]	[μm]	[cycle/mm]	[μm]	[μm]
36M-CT	100.2	5	117.7	4.2	3.07
10M-CT	42.4	11.8	48.2	10.4	5.87

After image reconstruction in CT, Fig. 5(a) and (e) respectively present tomographic slices of the lung specimen taken at x-ray energies of 20 and 25 keV. The specimen in the cylindrical body of the acrylic case with 36-mm outer diameter is depicted by the large FOV imaging. Fig. 5(b) depicts an enlarged image of the area enclosed by the yellow square in Fig. 5(a). Fig. 5(c and d) portray further enlarged images of the areas enclosed respectively by the right and left squares in Fig. 5(b). Similarly, Fig. 5(f and (g and h)), respectively portray enlarged images of the areas enclosed by the yellow squares in Fig. 5(e) and (f). Finally, Fig. 5(c, d, g, and h) depict individual alveoli of about 200 μm diameter. In the numerous alveoli of the lung, gases are exchanged with surrounding capillaries of diameter less than 10 μm. Each alveolus, with mean size of 200 μm, is shown clearly in the images. Each is not round but polygonal, resembling a cell of a honeycomb. The alveolar wall thickness is about 10 μm, which is nearly equal to the capillary diameter. In Fig. 5(c, d, g, and h), red arrows indicate specific spots with higher pixel values than those of the surrounding lung tissues. The specific spots correspond to cross-sections of small blood vessels filled with the contrast agent, which has high absorbance efficiency to x-rays. However, blue arrows indicate the streak artifacts caused by the presence of strongly attenuating objects similarly to tungsten wires in Fig. 2.

4. Discussion

Distortion correction operations were unnecessary before the CT reconstruction operation in the 36M-pixel CT system. For practical cone-beam three-dimensional CT implementations, distortion correction for all projection angles is necessary [33,34]. X-ray image intensifiers used for the cone-beam CT exhibit characteristic distortion that is attributable to both external and internal factors. However, the lenses used for commercial single-lens reflex cameras have negligibly small distortion.

Regarding the spatial resolutions, the 36M-pixel CT attained much higher performance in a cost effective manner than that achieved with the former 10M-pixel CT using the scientific grade CCD camera in Fig. 4 and Table 3. The spatial resolution of the 36M-pixel CT is 4.2 μm (MTF 5 %) in Table 3. The resolution value might visualize capillaries in the alveolar walls. Moreover, advancement of consumer grade camera technology is faster than that of scientific grade camera technology because consumer-grade camera manufacturers have larger R&D systems and commodity markets than those of scientific-grade camera firms. The 36M-pixel camera was released in April 2012. Five years later in September 2017, a new 45M-pixel camera (D850; Nikon Corp., Tokyo, Japan) was released. The present 36M-pixel camera includes a conventional front-illuminated CMOS sensor, but the new camera includes a high-sensitivity back-illuminated CMOS sensor. According to camera specifications, the 45M-pixel camera has a maximum camera ISO setting value of 25,600; that of the 36M-pixel camera is 6,400. A new micro-CT system using the 45M-pixel camera is under development [35]. Assembly of a new detector component is simple because the assembly method involves merely exchanging the D800e camera with a D850 camera.

As for the tomographic image quality, micro-CT imaging was performed at x-ray energies of 20 and 25 keV to evaluate x-ray energy dependence. Fig. 5 presents single tomographic slices of the lung specimen. The specimen in the cylindrical body of the acrylic case with 36-mm outer diameter is depicted by large FOV imaging in Fig. 5(a and e) taken respectively at energies of 20 and 25 keV. Fig. 5(b and f) depict
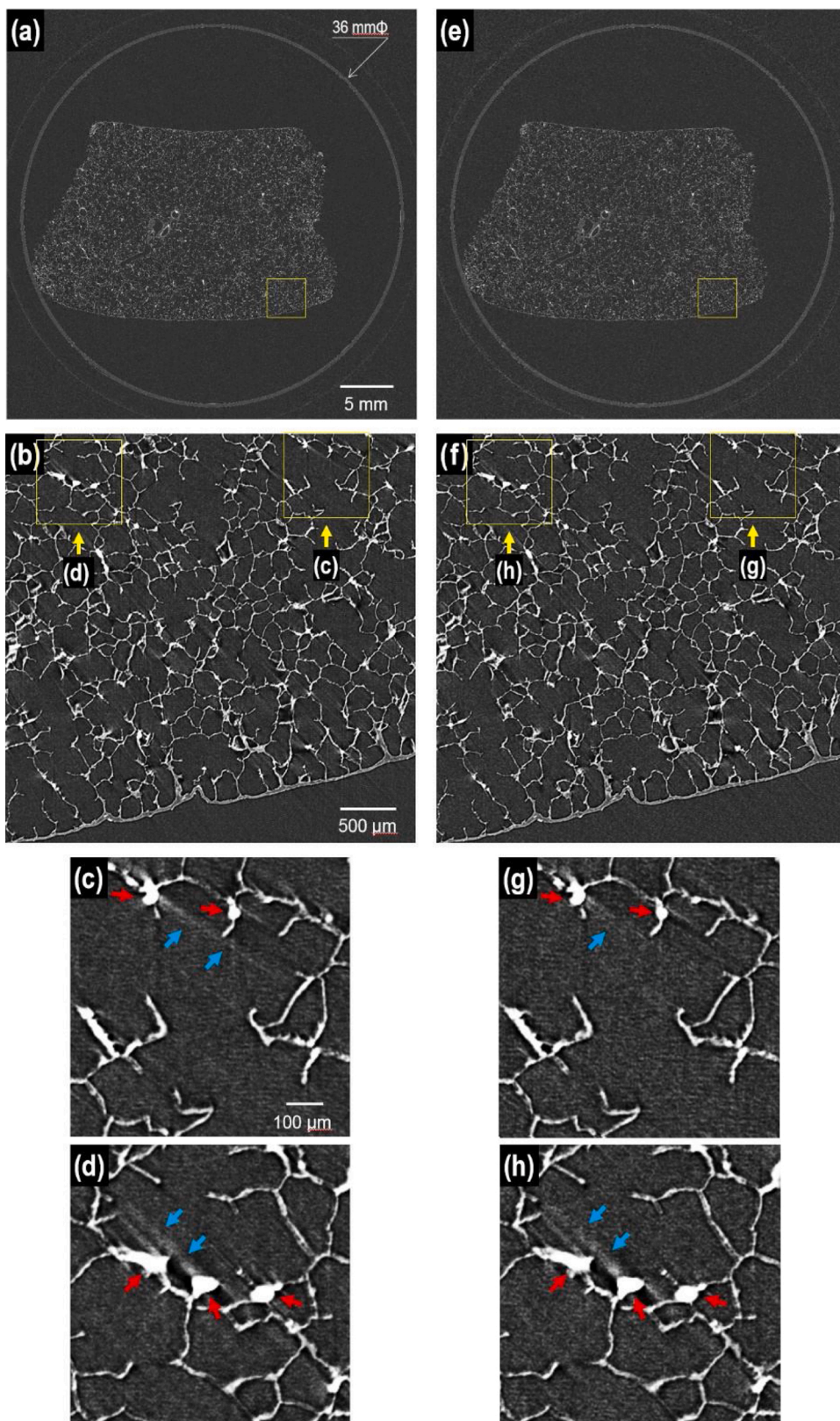
Fig. 5. Tomographic slices of the entire lung specimen taken at x-ray energies of (a) 20 keV and (e) 25 keV. (b) Enlarged image of the area enclosed by the yellow rectangle in (a). (c and d) Enlarged images of the areas enclosed respectively by the right and left rectangles in (b). Thereafter, similarly (f) and ((g) and (h)), respectively portray enlarged images of the areas enclosed by the yellow rectangles in (e) and (f). (For interpretation of the references to colour in the Figure, the reader is referred to the web version of this article).

enlarged images of the area enclosed by the yellow squares in Fig. 5(a and e), respectively, portraying individual alveoli of about 200 μm diameter.

Regarding the micro-wire phantom imaging in Fig. 2, the bright and dark streaks appeared at the x-ray energy of 15 keV. However, a 20 keV x-ray, a higher-energy x-ray, can prevent streak artifacts from occurring during MTF measurements [28]. In contrast, little difference exists between the specimen images in Fig. 5(a) and (e) and between Fig. 5(b) and (f) taken respectively at energies of 20 and 25 keV. However, the specimen images reveal differences when further enlarged. The streak

artifacts are indicated by blue arrows in Fig. 5(c) and (g). The streak indicated by the two blue arrows in Fig. 5(c) was changed into the streak indicated by the single blue arrow in Fig. 5(g). The 25 keV x-ray, a higher-energy x-ray, can reduce the streaks to some degree. The streak indicated by the two blue arrows in Fig. 5(d) was not changed in Fig. 5 (h). The specific spots indicated by the red arrows in Fig. 5(c and g) are smaller than those in Fig. 5(d and h). The specific spots correspond to cross-sections of blood vessels filled with the contrast agent. The artifact generated by small blood vessels in Fig. 5(c) was reduced using the higher-energy x-ray in Fig. 5(g), but the artifact generated by large blood vessels in Fig. 5(d) was not reduced in Fig. 5(h) because the higher-energy x-ray can no longer reduce the streak when the x-ray absorbance of the large vessels is too high. A readily apparent means of preventing streak artifacts is usage of low-density contrast agents to decrease the x-ray absorbance. In this study, the barium sulfate solution was administered to lung vessels as the contrast agent. The barium sulfate solution is suspended in buffer saline. For further dilution, buffer saline can be added to the suspension. In this way, the streak artifacts are reduced, even at the x-ray energy of 20 keV, to improve the tomographic image quality.

5. Conclusions

The present 36M-pixel CT using a consumer-grade single-lens reflex camera attained much higher performance in a cost-effective manner compared with the former 10M-pixel CT using the scientific grade CCD camera. The 36M-pixel CT, which has spatial resolution of 4.2 μm, can visualize capillaries in the alveolar walls using further diluted barium sulfate contrast agents. Recognition of the abnormalities reaching the capillary anatomy of the alveolar walls can engender clarification of the relation between the architectures and abnormalities related to lung disease mechanisms.

Funding

Declaration of Competing Interest

The authors report no declarations of interest.

Acknowledgments

References

[1] H. Itoh, K. Murata, J. Konishi, K. Nishimura, M. Kitaichi, T. Izumi, Diffuse lung disease: pathologic basis for the high-resolution computed tomography findings, J. Thorac. Imaging 8 (1993) 176–188.

[2] H. Itoh, M. Nishino, H. Hatabu, Architecture of the lung: morphology and function, J. Thorac. Imaging 19 (2004) 221–227, https://doi.org/10.1097/01.rti.0000142835.06988.b0.

[3] W.R. Webb, Thin-section CT of the secondary pulmonary lobule: anatomy and the image – the 2004 fleischner lecture, Radiology 239 (2006) 322–338, https://doi.org/10.1148/radiol.2392041968.

[4] Y. Kawata, N. Niki, K. Umetani, Y. Nakano, H. Ohmatsu, N. Moriyama, H. Itoh, Stochastic tracking of small pulmonary vessels in human lung alveolar walls using synchrotron radiation micro CT images, Proc. SPIE 8672 (2013), 867211, https://doi.org/10.1117/12.2006895. Medical Imaging.

[5] D. Haberthür, S.F. Barré, S.A. Tschanz, E. Yao, M. Stampanoni, J.C. Schittny, Visualization and stereological characterization of individual rat lung acini by high-resolution x-ray tomographic microscopy, J. Appl. Physiol. 115 (2013) 1379–1387, https://doi.org/10.1152/japplphysiol.00642.2013.

[6] E.R. Heitzman, The Lung: Radiologic–Pathologic Correlations, Mosby, St. Louis, MO, USA, 1984.

[7] H. Ikura, K. Shimizu, J. Ikezoe, T. Nagareda, N. Yagi, In vitro evaluation of normal and abnormal lungs with ultra-high-resolution CT, J. Thorac. Imaging 19 (2004) 8–15, https://doi.org/10.1097/00005382-200401000-00002.

[8] A. Tsuda, N. Filipovic, D. Haberthür, R. Dickie, Y. Matsui, M. Stampanoni, J.C. Schittny, Finite element 3D reconstruction of the pulmonary acinus imaged by synchrotron x-ray tomography, J. Appl. Physiol. 105 (2008) 964–976, https://doi.org/10.1152/japplphysiol.90546.2008.

[9] Y. Kawata, K. Kageyama, N. Niki, K. Umetatni, K. Yada, H. Ohmatsu, N. Moriyama, H. Itoh, Microstructural analysis of secondary pulmonary lobule imaged by synchrotron radiation micro CT using offset scan mode, Proc. SPIE 7626 (2010), 762610, https://doi.org/10.1117/12.845583. Medical Imaging.

[10] K. Umetani, K. Uesugi, M. Kobatake, A. Yamamoto, T. Yamashita, S. Imai, Synchrotron radiation microimaging in rabbit models of cancer for preclinical testing, Nucl. Instr. and Meth. A609 (2009) 38–49, https://doi.org/10.1016/j.nima.2009.07.058.

[11] H. Fan, H.L. Durko, S.K. Moore, J. Moore, B.W. Miller, L.R. Furenlid, S. Pradhan, H.H. Barrett, DR with a DSLR: digital radiography with a digital single-lens reflex camera, Proc. SPIE 7622 (2010), 76225E, https://doi.org/10.1117/12.844056. Medical Imaging.

[12] N.M. Winch, A. Edgar, X-ray imaging using a consumer-grade digital camera, Nucl. Instr. and Meth. A654 (2011) 308–313, https://doi.org/10.1016/j.nima.2011.06.087.

[13] A.R. Mistry, D. Uzbelger Feldman, J. Yang, E. Ryterski, Low dose x-ray sources and high quantum efficiency sensors: the next challenge in dental digital imaging? Radiol. Res. Pract. 2014 (2014), 543524 https://doi.org/10.1155/2014/543524.

[14] H. Xiang Fan, Lens-Coupled X-Ray Imaging Systems, Ph.D. Dissertation, the University of Arizona, Tucson, AZ, USA, 2015.

[15] K. Umetani, Y. Kawata, N. Niki, Development of 36M-pixel x-ray detector for large field of view and high-resolution micro-CT, Proc. SPIE 10020 (2016), 10020005, https://doi.org/10.1117/12.2246186. Photonics Asia.

[16] K. Umetani, H. Itoh, Y. Kawata, N. Niki, High-resolution wide-field synchrotron radiation micro-CT for large human lung specimen imaging, Proc. SPIE 10816 (2018), 108160A, https://doi.org/10.1117/12.2501282. Photonics Asia.

[17] M.D. Bentley, S.M. Jorgensen, L.O. Lerman, E.L. Ritman, J.C. Romero, Visualization of three-dimensional nephron structure with microcomputed tomography, Anat. Rec. 290 (2007) 277–283, https://doi.org/10.1002/ar.20422.

[18] E. Stolz, M. Yeniguen, M. Kreisel, M. Kampschulte, S. Doenges, D. Sedding, E.L. Ritman, T. Gerriets, A.C. Langheinrich, Angioarchitectural changes in subacute cerebral venous thrombosis. A synchrotron-based micro- and nano-CT study, Neuroimage 54 (2011), https://doi.org/10.1016/j.neuroimage.2010.10.056, 1881–1886.

[19] C.C. Chien, H.H. Chen, S.F. Lai, K.C. Wu, X. Cai, Y. Hwu, C. Petibois, Y. Chu, G. Margaritondo, Gold nanoparticles as high-resolution X-ray imaging contrast agents for the analysis of tumor-related micro-vasculature, J. Nanobiotechnol. 10 (2012) 10, https://doi.org/10.1186/1477-3155-10-10.

[20] J. Hu, Y. Cao, T. Wu, D. Li, H. Lu, High-resolution three-dimensional visualization of the rat spinal cord microvasculature by synchrotron radiation micro-CT, Med. Phys. 41 (2014), 101904, https://doi.org/10.1118/1.4894704.

[21] N. Niki, Y. Kawata, M. Fujii, R. Kakinuma, N. Moriyama, Y. Tateno, E. Matsui, Image analysis of pulmonary nodules using micro CT, Proc. SPIE 4322 (2001) 718–725, https://doi.org/10.1117/12.431149.

[22] F. Jian, L. Hongnian, L. Bing, Z. Lei, S. Jingjing, X-CT imaging method for large objects using double offset scan mode, Nucl. Instr. and Meth. A575 (2007) 519–523, https://doi.org/10.1016/j.nima.2007.03.008.

[23] D. Haberthür, C. Hintermüller, F. Marone, J.C. Schittny, M. Stampanoni, Radiation dose optimized lateral expansion of the field of view in synchrotron radiation x-ray tomographic microscopy, J. Synchrotron Rad. 17 (2010) 590–599, https://doi.org/10.1107/S0909049510019618.

[24] Z. Tang, R. Grompone von Gioi, P. Monasse, J.M. Morel, High-precision camera distortion measurements with a "calibration harp", J. Opt. Soc. Am. A 29 (2012) 2134–2143, https://doi.org/10.1364/JOSAA.29.002134.

[25] C.J. Bishof, J.C. Ehrhardt, Modulation transfer function of the EMI CT head scanner, Med. Phys. 4 (1977) 163–167, https://doi.org/10.1118/1.594305.

[26] E.L. Nickoloff, R. Riley, A simplified approach for modulation transfer function determinations in computed tomography, Med. Phys. 12 (1985) 437–442, https://doi.org/10.1118/1.595706.

[27] P.A. Assimakopoulos, D.P. Boyd, W. Jaschke, M.J. Lipton, Spatial resolution analysis of computed tomographic images, Invest. Radiol. 21 (1986) 260–271, https://doi.org/10.1097/00004424-198603000-00012.

[28] Y. Kawata, K. Kageyama, Y. Nakaya, N. Niki, K. Umetani, K. Yada, H. Ohmatsu, K. Eguchi, M. Kaneko, N. Moriyama, Measurement of spatial and density resolutions in X-ray nano-computed tomography, Proc. SPIE 7258 (2009), 725809, https://doi.org/10.1117/12.811323. Medical Imaging.

[29] Y. Nakaya, Y. Kawata, N. Niki, K. Umetani, H. Ohmatsu, N. Moriyama, A method for determining the modulation transfer function from thick microwire profiles measured using x-ray microcomputed tomography, Med. Phys. 39 (2012) 4347–4364, https://doi.org/10.1118/1.4729711.

[30] A.C. Kak, M. Slaney, Principles of Computerized Tomographic Imaging, IEEE Press, 1988.

[31] N. Haramati, R.B. Staron, K. Mazel-Sperling, K. Freeman, E.L. Nickoloff, C. Barax, F. Feldman, CT scans through metal scanning technique versus hardware composition, Comput. Med. Imaging Graph. 18 (1994) 429–434, https://doi.org/10.1016/0895-6111(94)90080-9.

[32] B. De Man, J. Nuyts, P. Dupont, G. Marchal, P. Suetens, Reduction of metal streak artifacts in x-ray computed tomography using a transmission maximum a posteriori

algorithm, IEEE Trans. Nucl. Sci. 47 (2000) 977–981, https://doi.org/10.1109/23.856534.

[33] R.R. Liu, S. Rudin, D.R. Bednarek, Super-global distortion correction for a rotational C-arm x-ray image intensifier, Med. Phys. 26 (1999) 1802–1810, https://doi.org/10.1118/1.598684.

[34] L.F. Gutiérrez, C. Ozturk, E.R. McVeigh, R.J. Lederman, A practical global distortion correction method for an image intensifier based x-ray fluoroscopy system, Med. Phys. 35 (2008) 997–1007, https://doi.org/10.1118/1.2839099.

[35] K. Umetani, D.O. Schwenke, J.T. Pearson, M. Shirai, T. Okamoto, Y. Kawata, N. Niki, Biomedical micro-CT and micro-angiography systems using high megapixel digital single-lens reflex cameras and synchrotron radiation, Proc. Tenth International Conference on Biomedical Engineering and Technology (2020) 128–134, https://doi.org/10.1145/3397391.3397448.